

Deformation effect on nuclear density profile and radius enhancement in light- and medium-mass neutron-rich nuclei

Wataru Horiuchi¹ and Tsunenori Inakura²

¹*Department of Physics, Hokkaido University, Sapporo 060-0810, Japan*

**E-mail: whoriuchi@nucl.sci.hokudai.ac.jp*

²*Laboratory for Advanced Nuclear Energy, Institute of Innovative Research, Tokyo Institute of Technology, Tokyo 152-8550, Japan*

.....
 Mass number dependence of the nuclear radii is closely related to the nuclear matter properties. It is known that the most of nuclei exhibit some deformation. We discuss how the nuclear density profile is modified by the nuclear deformation to elucidate the enhancement mechanism of the nuclear radii through a systematic investigation of neutron-rich Ne, Mg, Si, S, Ar, Ti, Cr, and Fe isotopes. Skyrme-Hartree-Fock calculations are performed in a three-dimensional Cartesian grid to describe the nuclear deformation in a non-empirical way. The role of the nuclear deformation on the nuclear density profiles is explored in comparison to calculations with spherical limit. We find correlations between the nuclear deformation and the internal nuclear density. The evolution of the nuclear radii appears to follow the core swelling mechanism recently proposed in spherical nuclei [Phys. Rev. C **101**, 061301(R) (2020)], and the radius is further enhanced by the nuclear deformation. This study demands further theoretical and experimental investigations for the internal density.

Subject Index xxx, xxx

arXiv:2106.13454v1 [nucl-th] 25 Jun 2021

1 Introduction

The nuclear landscape has been extended toward the neutron dripline and reached at Ne isotopes so far [1]. Following the discovery of new neutron-rich isotopes, the evolution of the nuclear radii in terms of the neutron excess has been of interest as it is closely related to the properties of “matter” composed of neutron and proton in such extreme neutron/proton ratio [2–7].

For stable nuclei, the mass number (A) dependence of the nuclear matter radius is roughly proportional to $A^{1/3}$ due to the saturation of the nuclear density [8, 9]. For neutron-rich unstable nuclei, many examples that deviate from this rule have been observed because of exotic structure properties, e.g., halo structure [10–12] and nuclear deformation [13, 14]. As it gets closer to the neutron dripline, emergence of deformed halo structure was predicted in Ne and Mg isotopes [15–20] and was actually observed for ^{31}Ne [21].

Recently, indications of the “core” swelling in neutron-rich Ca isotopes were reported [22, 23] exhibiting a kink of the charge and matter radii at $N = 28$. In Ref. [24], this phenomenon was related to the nuclear internal density that the “core” density swells to reduce the internal density for gaining the total energy. We remark that another mechanism to produce a kink of the charge radius for heavy nuclei was proposed in Ref. [25]. Since the most of nuclei are deformed [26], it is natural to extend the study of Ref. [24] for deformed neutron-rich nuclei.

The purpose of this paper is to clarify the radius enhancement mechanism of neutron-rich unstable nuclei, focusing on the role of the nuclear deformation. We study light- and medium-mass nuclei with the proton number $8 < Z < 28$, where their isotope dependence is significant. It is well known that the nuclear deformation considerably enhances the matter radius in light-mass neutron-rich isotopes, Ne and Mg [13, 14, 27–31]. We investigate how the density profiles are changed by the nuclear deformation and discuss its correlation with the internal density. Skyrme-Hartree-Fock (HF) calculations in the three-dimensional Cartesian coordinate are performed, which allow us to describe any deformed shape. Since the nuclear deformations predicted are strongly model dependent, several sets of standard Skyrme-type effective interactions are investigated.

The paper is organized as follows. Section 2 introduces the theoretical model employed in this paper. Model setups of the HF calculation to obtain the deformable ground-state wave functions is briefly explained. Section 3 is devoted to discuss changes of the density profiles and the enhancement mechanism of the nuclear radius due to nuclear deformation based on the HF results. We compare these results with spherical constrained HF to clarify the role of the nuclear deformation. Section 3.1 discusses the evolution of the nuclear deformation as a function of the neutron number for the neutron-rich isotopes with $8 < Z < 28$. Section 3.2

illuminates the deformation effect on the density profiles. We compare the density distributions obtained with the full and spherical constrained HF calculations for some selected nuclei, ^{34}Mg , ^{40}S , and ^{62}Cr . The role of nucleon orbits near the Fermi level is quantified. Section 3.3 describes more general discussions which relate the nuclear deformation and the nuclear density in the internal region. Finally, the conclusion is given in Sec. 4.

2 Skyrme Hartree-Fock calculation in three-dimensional coordinate space

In this paper, we employ the Skyrme-HF calculation. Since all details can be found in Refs. [24, 30, 32], we only give a minimum explanation for the present analysis. The ground-state wave function is expressed as the product of deformable single-particle (s.p.) orbits represented by the three-dimensional Cartesian mesh which is flexible enough to describe any nuclear deformation. We obtain these s.p. orbits fully self-consistently in the sphere of radius 20 fm based on the energy density functional of the intrinsic nucleon density $\tilde{\rho}$ [33], $E[\tilde{\rho}] = E_N + E_C - E_{\text{cm}}$, where E_N is the nuclear energy, E_C the Coulomb energy, and E_{cm} the center-of-mass energy. The total energy is minimized using the imaginary-time method [34]. The Coulomb interaction is incorporated as given in Ref. [35]. This paper aims to understand the nuclear deformation effect on the density profile, which is an extension of the previous study for spherical nuclei [24]. To obtain different density profiles, four kinds of Skyrme parameter sets, SkM* [36], SLy4 [37], SkI3 [38], and SIII [39] are employed. As a reference to clarify the role of the nuclear deformation, we also perform the spherical constrained HF calculation. To preserve the spherical symmetry, the self-consistent HF solution is obtained with the filling approximation [39], which assumes a uniform occupation of the Fermi level with angular momentum j as $m/(2j + 1)$ with m being the number of the outermost nucleons. We remark that the pairing correlation is an important ingredient for determining of the nuclear deformation. However, at this stage, the pairing correlation is ignored because it may induce further model dependence. See, e.g., [26, 40–43].

To guide the degree of the nuclear deformation, the quadrupole deformation parameter of the ground-state wave function is evaluated, which is defined by

$$\beta_2 = \sqrt{\beta_{20}^2 + \beta_{22}^2}, \quad (1)$$

where

$$\beta_{20} = \sqrt{\frac{\pi}{5}} \frac{\langle 2z^2 - x^2 - y^2 \rangle}{\langle r^2 \rangle}, \quad \beta_{22} = \sqrt{\frac{3\pi}{5}} \frac{\langle y^2 - x^2 \rangle}{\langle r^2 \rangle} \quad (2)$$

with $r^2 = x^2 + y^2 + z^2$. We take z as the quantization axis and choose it as the largest (smallest) principal axis for prolate (oblate) deformation. Thus, the sign of β_2 follows that

of β_{20} . The ground-state wave function can be triaxially deformed ($0 < \gamma < \pi/3$), which is treated as prolate ($0 < \gamma < \pi/6$) or oblate ($\pi/6 < \gamma < \pi/3$) for simplicity.

3 Results and discussions

3.1 Evolution of nuclear deformation

First we overview the neutron number dependence of even-even neutron-rich isotopes with $8 < Z < 28$. Among the four Skyrme-type interactions employed in this paper, the SkM* interaction is superior to describe the nuclear deformation and the validity of these density distributions for Ne and Mg isotopes were well evaluated as they showed good agreement with the measured cross sections [30, 44]. The results obtained with the SkM* interaction are mainly discussed unless otherwise mentioned.

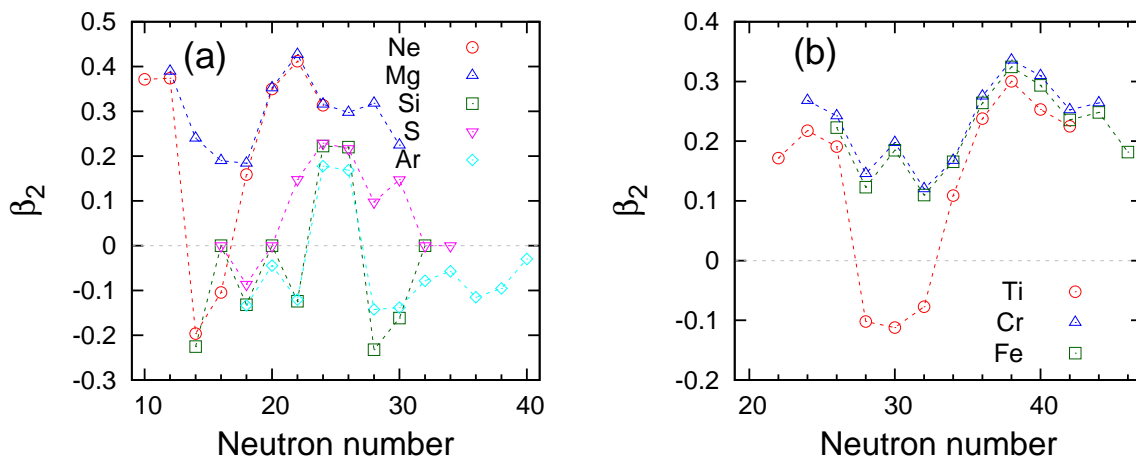


Fig. 1 Quadrupole deformation parameter of (a) Ne, Mg, Si, S, Ar, (b) Ti, Cr, and Fe isotopes as a function of the neutron number. The SkM* interaction is employed.

Figure 1 plots the quadrupole deformation parameter β_2 for those isotopes with (a) $8 < Z < 20$ and (b) $20 < Z < 28$ as a function of the neutron number. Let us first discuss the isotope dependence of the nuclear deformation for $8 < Z < 20$. The reader is referred to Ref. [30] for more discussions on the structure of those isotopes with $Z = 10$ –14. Actually, the nuclear deformation strongly depends on the proton and neutron numbers. The proton and neutron number of $Z, N = 10$ and 12 favor a prolately deformed state due to the occupation of the $[nn_z m_l] \tilde{\Omega} = [220]1/2$ and $[211]3/2$ orbits, where $n, n_z, m_l, \tilde{\Omega}$ denotes the asymptotic quantum numbers [46], the principal quantum number, that for the quantization axis z , the projection of the orbital angular momentum onto z , that of the total angular momentum

onto z , respectively. It is well known that Ne and Mg have large deformation in the island of inversion [14, 47–50]. The most of the Ne and Mg isotopes shows a prolate shape, whereas $^{24,26}\text{Ne}$ are oblately deformed.

To see the calculated results, the proton number of $Z = 14$ favors both the prolate and oblate states as the s.p. energy of the $[202]5/2$ orbit may compete with the prolately deformed orbits, e.g., $[220]1/2$ and $[211]3/2$. Competing with changes in the neutron shell structure by neutron excess, Si isotopes have relatively small deformations $|\beta_2| \lesssim 0.2$. The proton number of $Z = 16$ favors a spherical shape, and thus S isotopes have small β_2 values like Si isotopes. The most of the Ar isotopes ($Z = 18$) exhibit the oblate deformations. The nucleon number just before shell closure favors the oblate shape.

Figure 1 (b) draws β_2 of Ti, Cr, and Fe isotopes. The most of medium-mass nuclei have the prolate shape, which is known as the prolate dominance [51–53]. The oblate deformations are found only in $^{50-54}\text{Ti}$. ^{50}Ti forms the oblate shape which could be produced in the prolately deformed state coming from the combination of subshell closed neutron orbit ($N = 28$) and prolate-favoring $[330]1/2$ orbit ($Z = 22$). Ti, Cr, and Fe isotopes have large deformations at $N \approx 38$, where additional occupancy of the $[440]1/2$ and $[411]3/2$ orbits is induced like in the island of inversion found at $N \approx 20$.

3.2 Deformation effect on nuclear density profile

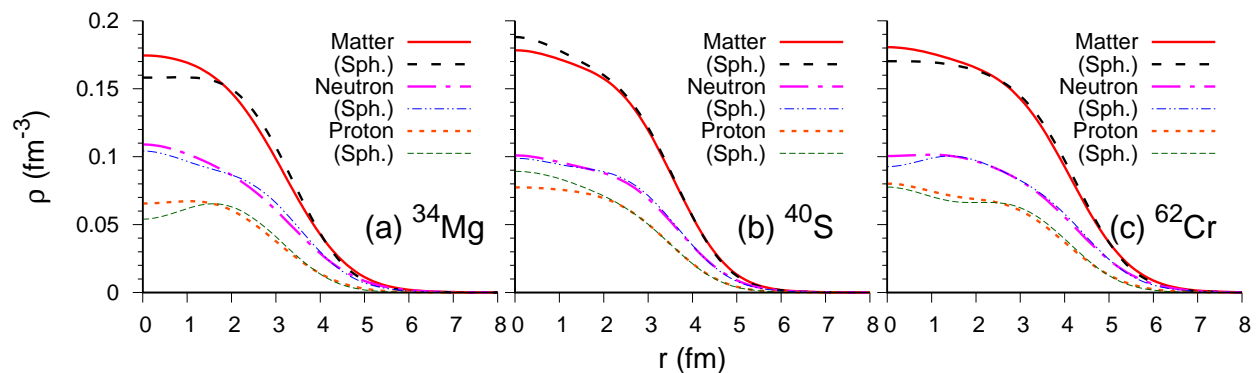


Fig. 2 Matter, neutron, and proton density distributions of (a) ^{34}Mg , (b) ^{40}S , and (c) ^{62}Cr obtained from the full and spherical (Sph.) HF calculations. The SkM* interaction is employed.

In this subsection, we show some specific examples how the density profile is modified by the nuclear deformation. Figure 2 displays those point-matter, neutron, and proton density

distributions of (a) ^{34}Mg , (b) ^{40}S , and (c) ^{62}Cr , which show the largest quadrupole deformation parameters for each isotope with the SkM* interaction. The deformed intrinsic density distributions are averaged over angles as $\rho(r) = \frac{1}{4\pi} \int d\Omega \tilde{\rho}(r, \Omega)$. The density distributions with the spherical constrained HF are also plotted for comparison. Compared to the spherical one, for ^{34}Mg and ^{62}Cr cases, the deformed state shows more diffused nuclear surface and higher internal density similarly to the case of ^{30}Ne [30], whereas for ^{40}S the internal density is reduced by the nuclear deformation.

These changes in the density profile crucially affect the total energy, which can be quantified by showing the cumulative energy per nucleon defined by

$$\varepsilon(r) = \int_0^r r'^2 dr' \int d\Omega E[\tilde{\rho}(r', \Omega)] / \int_0^r r'^2 dr' \int d\Omega \tilde{\rho}(r', \Omega). \quad (3)$$

Note that $\varepsilon(r)$ with $r \rightarrow \infty$ leads to the energy per nucleon $E[\tilde{\rho}]/A$. Figure 3 displays $\varepsilon(r)$ of the full and spherical constrained HF of (a) ^{34}Mg , (b) ^{40}S , and (c) ^{62}Cr . Significant contributions of the internal density, say below $\approx 2\text{--}3$ fm, can clearly be seen in the cumulative energies. The deformed nuclear states for ^{34}Mg and ^{62}Cr are more advantageous to gain the energy than the spherical nuclear states, while it is opposite in ^{40}S , where the nuclear internal density is reduced by the nuclear deformation. It should be noted that the deformed nuclear states always gain more energy than the spherical one in the surface regions beyond $\approx 3\text{--}4$ fm. The deformed state is selected in ^{40}S because the energy gain in the surface region is larger than the energy loss in the internal region compared to the spherical state.

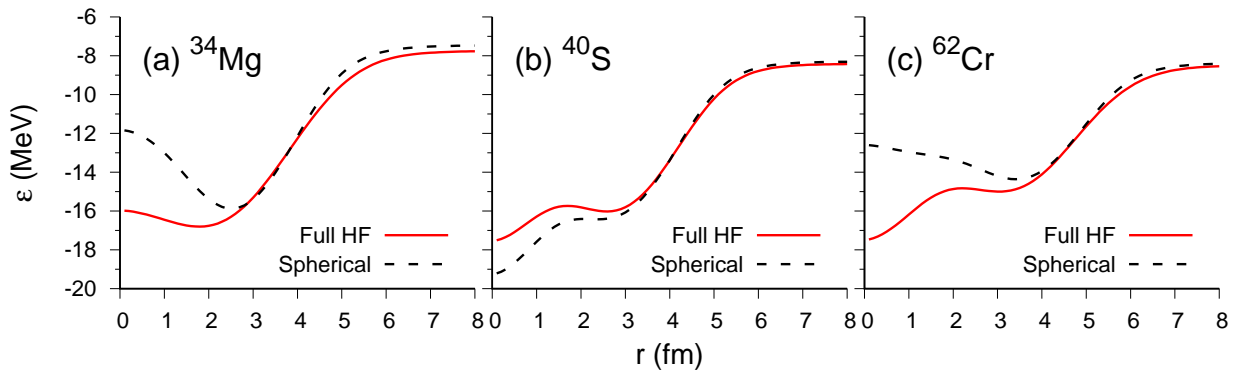


Fig. 3 Cumulative energies per nucleon of (a) ^{34}Mg , (b) ^{40}S , and (c) ^{62}Cr obtained from the full and spherical constrained HF calculations. The SkM* interaction is employed.

Since the characteristics of occupied s.p. orbit is crucial to determine the nuclear density distributions, we calculate the occupation probability of the spherical s.p. orbits for these deformed states. Practically, we simply take overlap between the s.p. orbits of the full and

spherical HF calculations. With this procedure, the components of the spherical s.p. orbits are projected out from each deformed s.p. orbit. The occupation probabilities for each spherical s.p. state are obtained by dividing those occupation numbers by the maximum occupation number $2j + 1$ for each s.p. state with the angular momentum j . Figure 4 displays these obtained occupation probabilities for neutron and proton of (a) ^{34}Mg , (b) ^{40}S , and (c) ^{62}Cr . The results with the spherical limit is also shown for comparison. The labels of the s.p. orbits are aligned in order of the s.p. energy. We see that the nuclear deformation only affects the distribution around the Fermi levels, which makes the surface more diffused due to the mixture of lower orbital-angular-momentum s.p. states, resulting in a further increase of the nuclear radius compared to the spherical limit. Regarding that these fully occupied orbitals belong to “core” of the nucleus, the structure change by the nuclear deformation is governed by the “valence” nucleons.

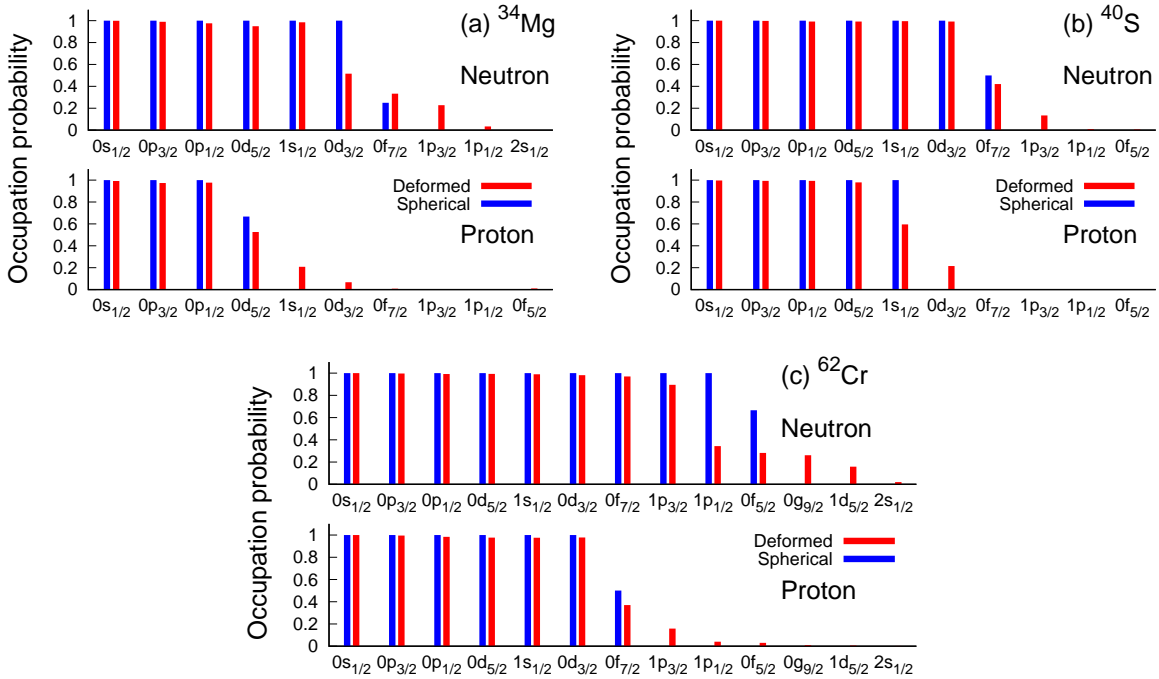


Fig. 4 Occupation probabilities of the full and spherical constrained HF single-particle (s.p.) orbits for (a) ^{34}Mg , (b) ^{40}S , and (c) ^{62}Cr . See text for details. The SkM* interaction is employed.

Let us discuss it in more detail. In (a) ^{34}Mg , since the $1s_{1/2}$ orbit is located just above the proton Fermi level $0d_{5/2}$, the nuclear deformation induces the occupancy of the $1s_{1/2}$ orbit, which leads to the enhancement of the central density as well as the nuclear diffuseness

as found in Fig. 2 (a). The same phenomenon is also found in the case of $N = 14$ isotones [54]. The nuclear deformation induces the occupancy of the $1s_{1/2}$ orbit and thus the central depression of the nuclear density disappears.

In contrast, in the case of (b) ^{40}S , the $1s_{1/2}$ orbit is fully occupied in the spherical limit. To get the state deformed, as the Fermi level for proton is $1s_{1/2}$, some of these protons should be moved to the other orbits around the Fermi level, i.e., the $0d_{3/2}$ orbit, resulting in the reduction of the $1s_{1/2}$ occupancy, i.e., the reduction of the central density compared to the spherical limit displayed in Fig. 2 (b).

For ^{62}Cr , the mechanism is not simple as these for ^{34}Mg and ^{40}S because no vacant or occupied s orbit near the Fermi level for both proton and neutron. Actually, the nuclear deformation induces a little increase of the occupancy of the $2s_{1/2}$ orbit for neutron. However, it is not enough to explain the enhancement of the central density presented in Fig. 2 (c). What induces the enhancement of the central density? To understand this, we compare the central densities that come from the deepest s.p. orbits $[000]1/2$ and $0s_{1/2}$ obtained by the deformed and spherical HF calculations, respectively. Since the full HF calculation produces a deeper mean-field potential than the spherical one, the $[000]1/2$ orbit is confined in a narrower potential well than that of the spherical $0s_{1/2}$ orbit. In fact, the respective s.p. energies are -44.41 and -43.29 MeV. The resulting central density of the $[000]1/2$ orbit for neutron becomes approximately 10% higher than the spherical $0s_{1/2}$ orbit, which corresponds to about half of the total enhancement of the central density. This enhancement of the central density for proton is tiny $\approx 1\%$. The other contribution may come from the change in the $1s_{1/2}$ orbit by the deformation, which is not easily identified as it is constructed from various deformed s.p. orbits.

We note that the pairing correlations also give the fractional occupation probabilities for the states around Fermi level. Incorporating the pairing interaction is necessary for more qualitative discussions that involve close comparison with experimental data, see, e.g., Ref. [45] for Cr isotopes; however, it is beyond the scope of this paper.

3.3 Correlations of the nuclear deformation and internal density

In the previous subsection, we showed the energy contributions of the internal and surface density, which can be the trigger for the nuclear deformation. Extending the discussion for more general cases, we evaluate the correlations between the nuclear deformation and the internal density. Here we take the central density $\rho(0) = \tilde{\rho}(0)$ as a degree of the internal density for all isotopes adopted in this paper.

Figure 5 (a) displays a correlation plot of the relative difference of the central densities calculated by the full and spherical constrained HF calculations: $\Delta[\rho(0)] = [\rho(0) -$

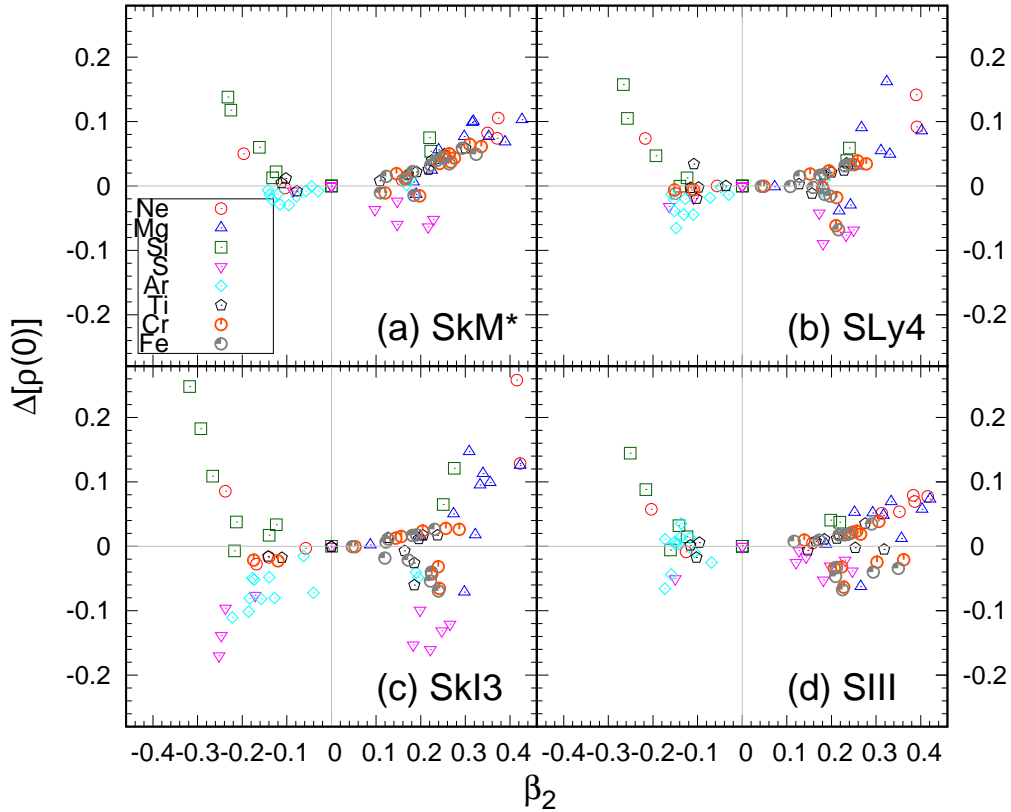


Fig. 5 Correlation plot of relative difference of the central densities between the full and spherical constrained HF calculations versus quadrupole deformation parameter β_2 of Ne, Mg, Si, S, Ar, Ti, Cr, and Fe isotopes. The (a) SkM*, (b) SLy4, (c) SkI3, and (d) SIII interactions are employed.

$\rho^{\text{sph.}}(0)]/\rho^{\text{sph.}}(0)$, with the SkM* interaction. We find that the $|\Delta[\rho(0)]|$ value becomes large for largely deformed states. This indicates that the nuclear deformation can be driven by those changes of the internal density. The most of isotopes are deformed by filling the internal densities, while the most of S, and Ar isotopes lower their internal densities by the nuclear deformation. The most striking difference of these isotopes among the others are that the central densities are quite high $\approx 0.18\text{--}0.19\text{ fm}^{-3}$ in the spherical limit because the $1s_{1/2}$ orbits are fully occupied like in the case of ^{40}S [Fig. 2 (b)].

We make the same analysis with the other Skyrme interactions, the SLy4, SkI3, and SIII interactions. The results are respectively displayed in Figs. 5 (b), (c) and (d). Though there are some quantitative differences, the similar trend is obtained for different Skyrme interactions. The larger $|\Delta[\rho(0)]|$, the larger $|\beta_2|$ becomes. The functional form of $|\Delta[\rho(0)]|$ appears to be a quadratic function of β_2 . To quantify this correlation, we calculate the correlation

coefficient of β_2^2 and $|\Delta[\rho(0)]|$ for each interaction. In fact, they show correlations as the calculated correlation coefficients are 0.77, 0.73, 0.66, and 0.54 for the SkM*, SLy4, SkI3, and SIII interactions, respectively. This square proportionality can roughly be explained within an assumption of volume conservation with a sharp radius R . Using the familiar radius formula $R' = R\sqrt{1 + (5/4\pi)\beta_2^2}$ [9] for quadrupole deformed surface for small β_2 , we get $\Delta[\rho(0)] \approx -\frac{15}{8\pi}\beta_2^2$. Though the estimation always predicts a negative value for $\Delta[\rho(0)]$, it gives $\Delta[\rho(0)] \approx -0.01$ – -0.05 for $|\beta_2| = 0.1$ – 0.3 , which is reasonable. In reality, the most of the cases show a positive $\Delta[\rho(0)]$ value owing to the modification of the surface distributions demonstrated in Figs. 2 (a) and (c). This rough estimation can only be applied to the cases that exhibit relatively small change of the surface density distributions, e.g., ^{40}S in Fig. 2 (b).

Comparing the results with different Skyrme interactions, the behavior of $\Delta[\rho(0)]$ with the SkM* and SLy4 interactions is similar; the largest $\Delta[\rho(0)]$ values are shown with the SkI3 interaction; and the SIII interaction tends to give smaller values and the correlation becomes small. This fact may be related to the nuclear equation of state (EOS) parameters, which characterize the softness of the nuclear matter against nucleon excess. Some relevant values for each interaction are listed in Table 1. Those listed EOS parameters are similar for the SkM* and SLy4 interactions. The SkI3 interaction has very large slope parameter of the symmetry energy L , while the incompressibility K_0 and the symmetry energy E_{sym} are not much different from these for the SkM* and SLy4 interactions. Since the energy loss against the neutron- and proton-number asymmetry from the nuclear saturation density, i.e., 0.16 fm^{-3} for $N = Z$, is largest for the SkI3 interaction, larger central density fraction $\Delta[\rho(0)]$ is needed to induce large nuclear deformation compared to the other interactions. In contrast, the SIII interaction gives extremely small L and large K_0 . As displayed in Fig. 5, the $\Delta[\rho(0)]$ values are hard to change compared to the other interactions.

Table 1 Saturation density, incompressibility, symmetry energy, and the slope parameter of the symmetry energy, of adopted Skyrme interactions. Energy is given in unit of MeV.

	$\rho_0 \text{ (fm}^{-3}\text{)}$	K_0	E_{sym}	L
SkM*	0.1602	216.40	30.04	45.80
SLy4	0.1595	229.90	32.00	45.94
SkI3	0.1577	257.96	34.83	100.49
SIII	0.1453	355.35	28.16	9.91

3.4 Evolution of the nuclear radius

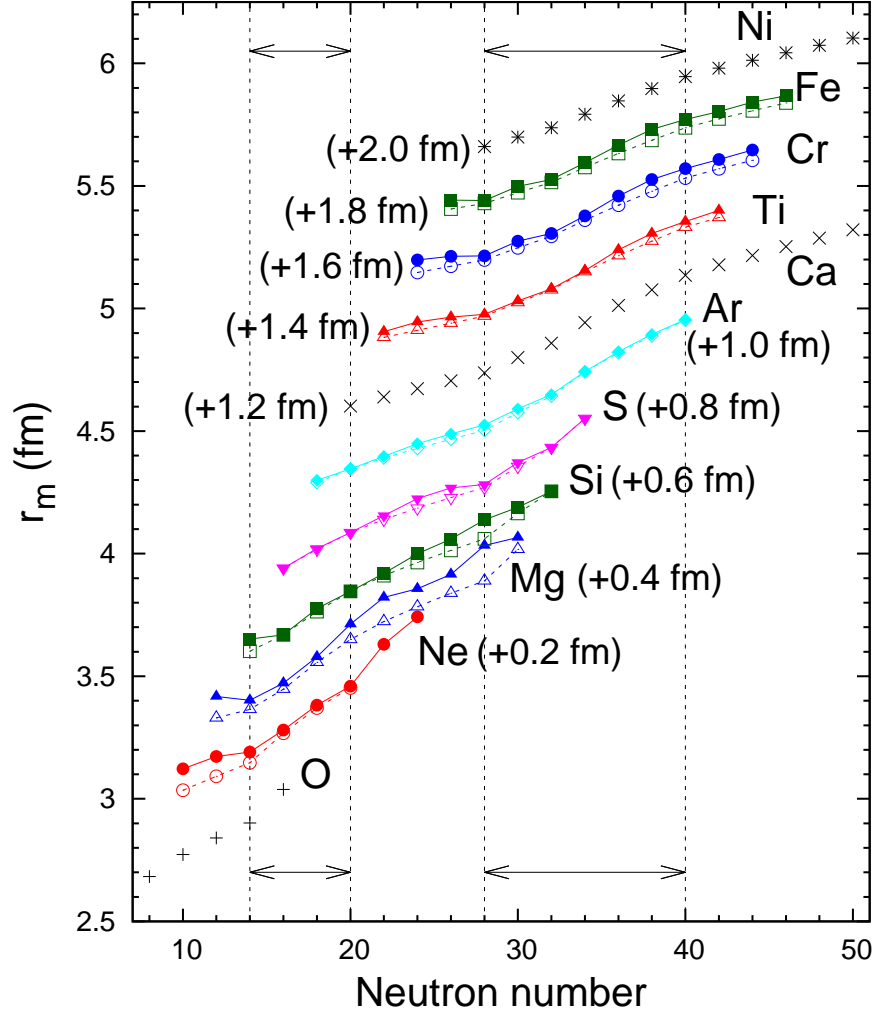


Fig. 6 Rms matter radii of O, Ne, Mg, Si, S, Ar, Ca, Ti, Cr, Fe, and Ni isotopes as a function of the neutron number. The open symbols denote the matter radii obtained with the spherical constraint HF calculations. The results of O, Ca, Ni are taken from Ref. [24]. For the sake of visibility, $(Z - 8) \times 0.1$ fm is added to the results. Two-headed arrows indicate the regions where the core swelling is expected to occur. See text for more details. The SkM* interaction is employed.

How does the nuclear deformation affect the nuclear radius? Figure 6 displays the root-mean-square (rms) matter radii r_m of those isotopes with $Z = 8-28$ calculated with the full (closed symbols) and the spherical constrained HF (open symbols) calculations. Note that we omit the results with the spherical HF calculations for $^{32,34}\text{Ne}$ because they are not bound.

A kink of the nuclear radius across $N = 18$ – 20 for Ne and Mg isotopes appears when the nuclear state exhibits large quadrupole deformation. The enhancement of the Ne isotopes near the dripline $N = 20$ – 24 is exception that can be recognized as the systems have weakly bound orbit $\lesssim 3$ MeV. They are consistent with the findings of the systematic analyses given in Refs. [27–31, 44].

We note that in the spherical constrained HF calculation despite that all the nuclear states are spherical, the matter radii already show some kinks at the magic and semi-magic numbers, i.e., $N = 14, 20,$ and 28 . This can be explained by the core swelling mechanism that recently proposed in Ref. [24]. The enhancement of the nuclear radii occurs when the valence neutrons fill the nodal or j -lower orbits, resulting in the core swelling or the enhancement of the nuclear radius to avoid the high density in the internal regions. For the sake of comparison, the results of the O, Ca, and Ni isotopes taken from Ref. [24] are shown. Their neutron number dependence is similar to those of the spherical constrained HF calculations from Ne to Fe isotopes studied in this paper: The sudden enhancement of the nuclear radius occurs in the spherical constrained HF calculations for $N = 14$ – 20 when $1s_{1/2}, 0d_{3/2}$ are occupied, and for $N = 28$ – 40 when $1p_{3/2}, 0f_{5/2},$ and $1p_{1/2}$ are occupied.

We see that the deformed HF results always gives larger radius than the spherical one for all the isotopes employed in this paper. It is natural to presume that the radius enhancement occurs by following the core swelling mechanism [24] and the radius is further enhanced when the nucleus exhibits the nuclear deformation.

4 Conclusions

In order to elucidate the enhancement mechanism of the nuclear radius, we have studied the effect of the nuclear deformation on the nuclear density profiles. A systematic investigation for even-even light- and medium-mass neutron-rich nuclei of $8 < Z < 28$ has been made based on the ground-state density distributions obtained from Skyrme-Hartree-Fock calculations in a three-dimensional Cartesian mesh. A spherical constrained HF calculation has also been performed as a reference state of each deformed HF state.

The nuclear internal density can be a key to understanding the deformation phenomena. We have shown that the nuclear deformation is determined by minimizing the total energy in the whole nuclear regions, not only in the surface region but also in the internal region. We find correlations between the changes in the internal density and the nuclear deformation, which can be related to the properties of nuclear matter. A deformed nuclear state is selected to weigh the relative energy gains in the internal and surface regions. In general, the nuclear

deformation induces more diffused nuclear surface while changing the magnitude of the density distributions in the internal regions. From a microscopic point of view, this phenomenon can be explained by considering the fact that the nuclear deformation mainly influences the occupation of the spherical single-particle orbits near the Fermi level. Changes of the nuclear density in the internal regions become significant when the occupied or unoccupied s orbital is located near the Fermi level because its occupation number is strongly modified by the nuclear deformation.

We have found that in the spherical limit the evolution of the nuclear radius with respect to the neutron number follows the core swelling rule proposed in Ref. [24] that a “core” nucleus swells when the single-particle orbits that have large spatial overlap between the orbitals in the core. The core swelling is responsible for developing the nuclear bulk and the nuclear deformation plays a role to diffuse the density profile at the surface regions resulting in a further increase of the nuclear radius. The nuclear deformation mainly changes the occupation number near the Fermi level, while the occupation numbers of the deeper bound orbitals are not changed even the single-particle states are deformed. This is a strong basis that the core swelling phenomena found in the spherical nuclei [23, 24] is universal for the radius enhancement, although the occupation number of the single-particle orbits near the Fermi level becomes fractional by the surface phenomena such as nuclear deformation.

In this paper, we have discussed the possible correlations between the nuclear deformation and internal density. We note, however, this work only includes the deformation effect to the density profile with a standard mean-field approximation. To establish the finding of this work, a careful investigation is necessary that includes the pairing correlation and various many-body effects beyond the mean-field level. Also, experimental studies to extract the internal density of unstable nuclei are desired such as electron scattering which was recently realized [55].

Acknowledgment

This work was in part supported by JSPS KAKENHI Grants No. 18K03635. We acknowledge the collaborative research program 2021, Information Initiative Center, Hokkaido University.

References

- [1] D. S. Ahn, N. Fukuda, H. Geissel, N. Inabe, N. Iwasa, T. Kubo, K. Kusaka, D. J. Morrissey, D. Murai, T. Nakamura *et al.*, Phys. Rev. Lett. **123**, 212501 (2019).
- [2] L. W. Chen, C. M. Ko, B. A. Li, and J. Xu, Phys. Rev. C **82**, 024321 (2010).
- [3] P.-G. Reinhard and W. Nazarewicz, Phys. Rev. C **81**, 051303(R) (2010).
- [4] X. Roca-Maza, M. Centelles, X. Viñas, and M. Warda, Phys. Rev. Lett. **106**, 252501 (2011).
- [5] M. Kortelainen, J. Erler, W. Nazarewicz, N. Birge, Y. Gao, and E. Olsen, Phys. Rev. C **88**, 031305(R) (2013).

- [6] T. Inakura, T. Nakatsukasa, and K. Yabana, *Phys. Rev. C* **88**, 051305(R) (2013).
- [7] X. Roca-Maza, X. Viñas, M. Centelles, B. K. Agrawal, G. Coló, N. Paar, J. Piekarewicz, and D. Vretenar, *Phys. Rev. C* **92**, 064304 (2015).
- [8] H. de Vries, C. W. de Jager, and C. de Vries, *Atomic Data and Nuclear Data Tables* **36**, 495 (1987).
- [9] A. Bohr and B. R. Mottelson, *Nuclear Structure, Vol. I* (W. A. Benjamin, New York, 1975).
- [10] I. Tanihata, H. Hamagaki, O. Hashimoto, Y. Shida, N. Yoshikawa, K. Sugimoto, O. Yamakawa, T. Kobayashi, and N. Takahashi, *Phys. Rev. Lett.* **55**, 2676 (1985).
- [11] I. Tanihata, H. Savajols, and R. Kanungo, *Prog. Part. Nucl. Phys.* **68**, 215 (2013), and references therein.
- [12] S. Bagchi, R. Kanungo, Y. K. Tanaka, H. Geissel, P. Doornenbal, W. Horiuchi, G. Hagen, T. Suzuki, N. Tsunoda, D. S. Ahn *et al.*, *Phys. Rev. Lett.* **124**, 222504 (2020).
- [13] M. Takechi, T. Ohtsubo, M. Fukuda, D. Nishimura, T. Kuboki, T. Kubo, T. Suzuki, T. Yamaguchi, A. Ozawa, T. Moriguchi, H. Ooishi, *Phys. Lett.* **707**, 357 (2012).
- [14] M. Takechi, S. Suzuki, D. Nishimura, M. Fukuda, T. Ohtsubo, M. Nagashima, T. Suzuki, T. Yamaguchi, A. Ozawa, T. Moriguchi *et al.*, *Phys. Rev. C* **90**, 061305(R) (2014).
- [15] H. Nakada, *Nucl. Phys.* **A 808**, 47 (2008).
- [16] S.-G. Zhou, J. Meng, P. Ring, and E.-G. Zhao, *Phys. Rev. C* **82**, 011301(R) (2010).
- [17] L. Li, J. Meng, P. Ring, E.-G. Zhao, and S.-G. Zhou, *Phys. Rev. C* **85**, 024312 (2012).
- [18] Y. N. Zhang, J. C. Pei, and F. R. Xu, *Phys. Rev. C* **88**, 054305 (2013).
- [19] H. Nakada and K. Takayama, *Phys. Rev. C* **98**, 011301(R) (2018).
- [20] H. Kasuya and K. Yoshida, *Prog. Theor. Exp. Phys.* **2021**, 013D01 (2021).
- [21] T. Nakamura, N. Kobayashi, Y. Kondo, Y. Satou, J. A. Tostevin, Y. Utsuno, N. Aoi, H. Baba, N. Fukuda, J. Gibelin *et al.*, *Phys. Rev. Lett.* **112**, 142501 (2014).
- [22] R. F. Garcia Ruiz, M. L. Bissell, K. Blaum, A. Ekström, N. Frömmgen, G. Hagen, M. Hammen, K. Hebeler, J. D. Holt, G. R. Jansen *et al.*, *Nat. Phys.* **12**, 594 (2016).
- [23] M. Tanaka, M. Takechi, M. Fukuda, D. Nishimura, T. Suzuki, Y. Tanaka, T. Moriguchi, D. S. Ahn, A. Aimaganbetov, M. Amano *et al.*, *Phys. Rev. Lett.* **124**, 102501 (2020).
- [24] W. Horiuchi and T. Inakura, *Phys. Rev. C* **101**, 061301(R) (2020).
- [25] H. Nakada, *Phys. Rev. C* **100**, 044310 (2019).
- [26] M. V. Stoitsov, J. Dobaczewski, W. Nazarewicz, S. Pittel, and D. J. Dean, *Phys. Rev. C* **68**, 054312 (2003).
- [27] K. Minomo, T. Sumi, M. Kimura, K. Ogata, Y. R. Shimizu, and M. Yahiro, *Phys. Rev. C* **84**, 034602 (2011).
- [28] K. Minomo, T. Sumi, M. Kimura, K. Ogata, Y. R. Shimizu, and M. Yahiro, *Phys. Rev. Lett.* **108**, 052503 (2012).
- [29] T. Sumi, K. Minomo, S. Tagami, M. Kimura, T. Matsumoto, K. Ogata, Y. R. Shimizu, and M. Yahiro, *Phys. Rev. C* **85**, 064613 (2012).
- [30] W. Horiuchi, T. Inakura, T. Nakatsukasa, and Y. Suzuki, *Phys. Rev. C* **86**, 024614 (2012).
- [31] S. Watanabe, K. Minomo, M. Shimada, S. Tagami, M. Kimura, M. Takechi, M. Fukuda, D. Nishimura, T. Suzuki, T. Matsumoto *et al.*, *Phys. Rev. C* **89**, 044610 (2014).
- [32] T. Inakura, H. Imagawa, Y. Hashimoto, S. Mizutori, M. Yamagami K. Matsuyanagi, *Nucl. Phys.* **A 768**, 61 (2006).
- [33] D. Vautherin and D. M. Brink, *Phys. Rev. C* **5**, 626 (1972).
- [34] K. T. R. Davies, H. Flocard, S. Krieger, and M.S. Weiss, *Nucl. Phys.* **A 342**, 111 (1980).
- [35] H. Flocard, S.E. Koonin, and M.S. Weiss, *Phys. Rev. C* **17**, 1682 (1978).
- [36] J. Bartel, P. Quentin, M. Brack, C. Guet, and H. Håkansson, *Nucl. Phys.* **A 386**, 79 (1982).
- [37] E. Chanbanat, P. Bonche, P. Haensel, J. Mayer, and R. Schaeffer, *Nucl. Phys.* **A 627**, 710 (1997).
- [38] P.-G. Reinhard and H. Flocard, *Nucl. Phys.* **A 584**, 467 (1995).
- [39] M. Beiner, H. Flocard, N. V. Giai, and Ph. Quentin, *Nucl. Phys.* **A 238**, 29 (1975).
- [40] J. -P. Delaroche, M. Girod, J. Libert, H. Goutte, S. Hilaire, S. Péru, N. Pillet, and G. F. Bertsch, *Phys. Rev. C* **81**, 014303 (2010).
- [41] S. A. Changizi and C. Qi, *Phys. Rev. C* **91**, 024305 (2015).
- [42] W. Horiuchi, S. Hatakeyama, S. Ebata, and Y. Suzuki, *Phys. Rev. C* **93**, 044611 (2016).
- [43] W. Horiuchi, S. Ebata, and K. Iida, *Phys. Rev. C* **96**, 035804 (2017).
- [44] W. Horiuchi, T. Inakura, T. Nakatsukasa, and Y. Suzuki, *JPS Conf. Proc.* **6**, 030079 (2015).
- [45] K. Yoshida and N. Hinohara, *Phys. Rev. C* **83**, 061302(R) (2011).
- [46] S. G. Nilsson, *Mat. Fys. Medd. Dan. Vid. Selsk.* **29**, pp.1-69 (1955).
- [47] X. Campi, H. Flocard, A.K. Kerman, S. Koonin, *Nucl. Phys.* **A 251**, 193 (1975).
- [48] C.Thibault, R. Klapisch, C. Rigaud, A. M. Poskanzer, R. Prieels, L. Lessard, and W. Reisdorf, *Phys. Rev. C* **12**, 644 (1975).
- [49] S. Nummela, F. Nowacki, P. Baumann, E. Caurier, J. Cederkäll, S. Courtin, P. Dessagne, A. Jokinen, A. Knipper, G. Le Scornet *et al.*, *Phys. Rev. C* **64**, 054313 (2001).

- [50] P. Doornenbal, H. Scheit, N. Aoi, S. Takeuchi, K. Li, E. Takeshita, H. Wang, H. Baba, S. Deguchi, N. Fukuda *et al.*, Phys. Rev. Lett. **103**, 032501 (2009).
- [51] K. Kumar, Phys. Rev. C **1**, 369 (1970).
- [52] N. Tajima and N. Suzuki, Phys. Rev. C **64**, 037301 (2001).
- [53] I. Hamamoto and B. R. Mottelson, Phys. Rev. C **79**, 034317 (2009).
- [54] V. Choudhary, W. Horiuchi, M. Kimura, and R. Chatterjee, Phys. Rev. C **102**, 034619 (2020).
- [55] K. Tsukada, A. Enokizono, T. Ohnishi, K. Adachi, T. Fujita, M. Hara, M. Hori, T. Hori, S. Ichikawa, K. Kurita *et al.*, Phys. Rev. Lett. **118**, 262501 (2017).